



Title	Optimization of combustion chamber geometry for natural gas engines with diesel micro-pilot-induced ignition
Author(s)	Wang, Bin; Li, Tie; Ge, Linlin; Ogawa, Hideyuki
Citation	Energy conversion and management, 122, 552-563 https://doi.org/10.1016/j.enconman.2016.06.027
Issue Date	2016-08-15
Doc URL	http://hdl.handle.net/2115/71310
Rights	© 2016. This manuscript version is made available under the CC-BY-NC-ND 4.0 license http://creativecommons.org/licenses/by-nc-nd/4.0/
Rights(URL)	http://creativecommons.org/licenses/by-nc-nd/4.0/
Type	article (author version)
File Information	Revised Manuscript-clean version.pdf



[Instructions for use](#)

1 Optimization of combustion chamber geometry for natural gas engines with
2 diesel micro-pilot-induced ignition

3 Bin Wang^{1,2}, Tie Li^{1,2*}, Linlin Ge¹, Hideyuki Ogawa³

4 1. State Key Laboratory of Ocean Engineering, Shanghai Jiao Tong University

5 2. Collaborative Innovation Center for Advanced Ship and Deep-Sea Exploration, Shanghai
6 Jiao Tong University

7 3. Faculty of Engineering, Hokkaido University

8 *Corresponding Address: 800 Dongchuan Rd., Shanghai, PR China, 200240;
9 Tel.: (86)21-3420-8348; *E-mail*: litie@sjtu.edu.cn

10 **ABSTRACT**

11 Smokeless, low nitrogen oxides (NO_x), and high thermal efficiency have been achieved through
12 the lean-burn concept for natural gas engine with diesel micro-pilot-induced ignition (MPII).
13 However, the combustion chamber is usually not specialized for natural gas combustion, and
14 increases in the unburned hydrocarbon (HC) and carbon monoxide (CO) emissions are still a
15 challenge for this type of engines. This paper describes optimization of the combustion chamber
16 geometry to reduce the HC and CO emissions and improve the combustion efficiency in the
17 MPII natural gas engine. The 3-D computational fluid dynamics (CFD) simulation model
18 coupled with a chemical reaction mechanism is described. The temporal development of the
19 short-pulsed diesel spray in a high pressure constant-volume vessel is measured and used to
20 calibrate the spray model in the CFD simulation. The simulation models are validated by the
21 experimental data of the in-cylinder pressure trace, apparent heat release rate (AHRR) and
22 exhaust gas emissions from a single-cylinder MPII natural gas engine. To generate the various
23 combustion chamber geometries, the bowl outline is parameterized by the two cubic Bezier

24 curves while keeping the compression ratio constant. The available design space is explored by
25 the multi-objective non-dominated sorting genetic algorithm II (NSGA-II) with
26 Kriging-based meta-model. With the optimization, the HC and CO emissions are reduced by
27 56.47% and 33.55%, respectively, while the NO_x emissions, the maximum rate of pressure rise
28 and the gross indicated thermal efficiency that are employed as the constraints are slightly
29 improved. Finally, the mechanism of the reduction in HC and CO emissions with the optimized
30 combustion chamber geometry is investigated and discussed in details.

31

32 **KEY WORDS:** natural gas, diesel micro-pilot-induced ignition, combustion chamber geometry,
33 HC/CO emissions, model-based optimization

34 **1. Introduction**

35 Due to the higher energy conversion efficiency than other power plants, the compression
36 ignition (CI) diesel engines are widely adopted as the primary propulsion device for ships [1, 2].
37 In order to restrict the harmful emissions from the commercial vessels, especially in the
38 designated emission control areas (ECAs), Tier III emission standard regulated by International
39 Maritime Organization (IMO) will be implemented in 2016 [3]. Compared to IMO Tier I, this
40 stage requires a reduction of the nitrogen oxides (NO_x) by 80%. Stricter limitations are also
41 progressively applied on the sulfur oxides (SO_x) and particulate matter (PM) emissions. To meet
42 the upcoming emission regulations, the alternative fuels together with advanced clean
43 combustion concepts will play an increasingly important role in the future transportation systems
44 with diesel engine as power source [4-6].

45 With development and maturity of the shale gas technology, the natural gas production in
46 America has increased substantially up to 31,345 billion cubic feet in 2014, which is 16.8%
47 larger than that in 2010 [7, 8]. Foreseeably, natural gas is becoming one of the promising
48 alternative fuels in the field of energy since it is available in greater quantities with lower cost. In
49 addition, natural gas also has the advantage of lower harmful emissions in comparison with the
50 traditional petroleum fuels (i.e., gasoline and diesel). Natural gas is mainly consisted of methane
51 (CH₄). With a promotion of natural gas application as fuels, the carbon dioxide (CO₂) and PM
52 emissions can be suppressed, as a result of the higher hydrogen to carbon (H/C) atom ratio in
53 natural gas. The research octane number (RON) of natural gas is up to about 130 [9]. Hence, the
54 higher compression ratio can be applied in the natural gas engines so as to obtain the better
55 thermal efficiency. Furthermore, natural gas has the wider flammable limit. Based on the

56 constant volume combustion chamber, Liao et al. [10] measured the lean flammable limit and
57 upper flammable limit for the natural gas/air mixtures were 5% and 15.6%, respectively, of
58 natural gas by volume. Therefore, the lean-burn combustion concept with increasing boost
59 pressure is available for the natural gas engines in order to obtain the excellent comprehensive
60 characteristics of the fuel economy, power performance and exhaust gas emissions.

61 Recently, several researchers have investigated the various applications of natural gas in the
62 internal combustion engines with a focus on the characteristics of the performance, combustion
63 and exhaust gas emissions. Due to the low self-ignitability, natural gas has been usually utilized
64 in the spark ignition (SI) engines [11]. In general, this kind of the technical scheme was adopted
65 to replace the gasoline engine in some automobiles because of the cheaper price and lower
66 emissions [12]. Nonetheless, Ogawa et al. [13] reported that the advantages of natural gas would
67 not be completely explored in the SI engines and the reduction of engine power performance
68 was remarkable. As to the CI engines, the dual fuel operating mode of natural gas coupled with
69 the high reactivity fuel (e.g., diesel fuel) provides the novel opportunity and application mode
70 [13, 14]. Under the high compression ratio conditions, the micro-pilot diesel was injected into
71 the cylinder to ignite the premixed natural gas. Takahashi et al. [15] proposed a dual fuel
72 combustion strategy of natural gas/diesel in the marine engine with a pre-combustion chamber.
73 The small amount of diesel fuel, which is about 1% of total input energy, was injected into the
74 pre-combustion chamber. The natural gas in the pre-combustion chamber was ignited firstly,
75 then the flame propagated into the main cylinder to burn the lean pre-mixture of the natural gas
76 and air. The released energy by those small quantity of diesel fuel as an ignition source was
77 thousands of times more powerful than that of a normal spark plug. Hence, this kind of the

78 ignition mode is more reliable and stable even under the high compression ratio and ultra-lean
79 mixture conditions. Furthermore, the technique that the diesel fuel is directly injected in the
80 cylinder will be more flexible than that of the above-mentioned pre-combustion chamber scheme.
81 In the gas engine KU30GA, the natural gas as a main fuel was supplied from the intake manifold
82 system, while the micro-pilot diesel fuel was directly injected in the cylinder to control the
83 combustion phasing [16]. Besides the simpler arrangement and quicker launch, it is also a
84 practical way to take advantage of natural gas more efficiently in the CI engines.

85 Natural gas engines with the micro-pilot diesel ignition can significantly reduce NO_x and
86 PM emissions [13, 17]. However, the unburned hydrocarbon (HC) and carbon monoxide (CO)
87 emissions are obviously higher than that of the normal diesel mode [18]. Yousefi et al. [5]
88 established a multi-dimensional computational fluid dynamics (CFD) model coupled with the
89 chemical kinetics mechanisms to examine the effect of various premixed fuels including natural
90 gas and equivalence ratios on the performance and emissions of a dual-fuel pilot diesel ignition
91 engine. Liu et al. [19] presented the effects of pilot fuel quantity on the emissions characteristics
92 of a natural gas/diesel dual fuel engine. Under the lean premixed conditions, NO_x emissions can
93 be reduced by 30% in comparison to the baseline diesel engine. In addition, the authors claimed
94 that the unburned methane accounts for about 90% of the HC emissions, while the CO emissions
95 are originated mainly from the quenching of the lean premixed natural gas mixture. Ishiyama et
96 al. [20] studied the different diesel pilot injection timings for improvement of the dual-fuel
97 combustion with a lean natural gas-air mixture. As to the single-stage injection experiments, the
98 results showed that the injection timings from -20° to -10° CA ATDC produce the low HC/CO
99 emissions. The earlier injection at -35° CA ATDC is advantageous to reduce NO_x; but it

100 deteriorates the HC/CO emissions. The two-stage pilot injections with an early first injection and
101 a moderately advanced second injection enable the improved thermal efficiency and reduced
102 exhaust emissions. Based on a single-cylinder direct injection CI engine, Abdelaal and Hegab
103 [17] focused on the partly-cooled exhaust gas recirculation (EGR) to achieve higher thermal
104 efficiency and lower exhaust emissions, particularly at part loads. Dual-fuel mode with moderate
105 EGR, such as 5%, 10%, and 20%, exhibits the thermal efficiency comparable to the conventional
106 diesel mode. The larger reduction of NO_x can be achieved, when the higher percentage of EGR
107 is employed. The application of EGR to dual-fuel mode slightly reduces the HC and CO
108 emissions, but these emissions were still considerably higher than that of the conventional diesel
109 engine.

110 The dual fuel engines in the previous studies are mostly realized by modifying the
111 conventional diesel engines with the natural gas introduced into the intake ports. While the
112 combustion chamber geometry plays a critical role in the combustion, so far few researches
113 focus on the effect of combustion chamber geometry on the performance and exhaust gas
114 emissions of the dual fuel natural gas engine. Such a study is particularly necessary for the MPII
115 engines with the natural gas as the main fuel and the micro-pilot diesel primarily as an ignition
116 source, since the combustion in the MPII engines could be totally different from the
117 conventional diesel diffusive combustion. Therefore, it is necessary to explore the potential of
118 optimized combustion chamber for the MPII concept to reduce the HC and CO emissions and
119 improve the energy conversion efficiency.

120 The objective of this study is to investigate the potential of optimizing the combustion
121 chamber geometry to reduce the HC and CO emissions and further improve the energy

122 conversion efficiency of the MPII natural gas engine. The paper is organized as follows: the
123 experimental setups of the bench test of an MPII natural gas engine and a spray visualization
124 system are firstly described. Then, the numerical models based on 3D computational fluid
125 dynamics for the MPII engine are formulated and calibrated against the spray visualization and
126 engine bench test data, followed by the model-based optimization methodology for the
127 combustion chamber design. After the presentation of the results and detailed discussion, finally,
128 the major conclusions are summarized.

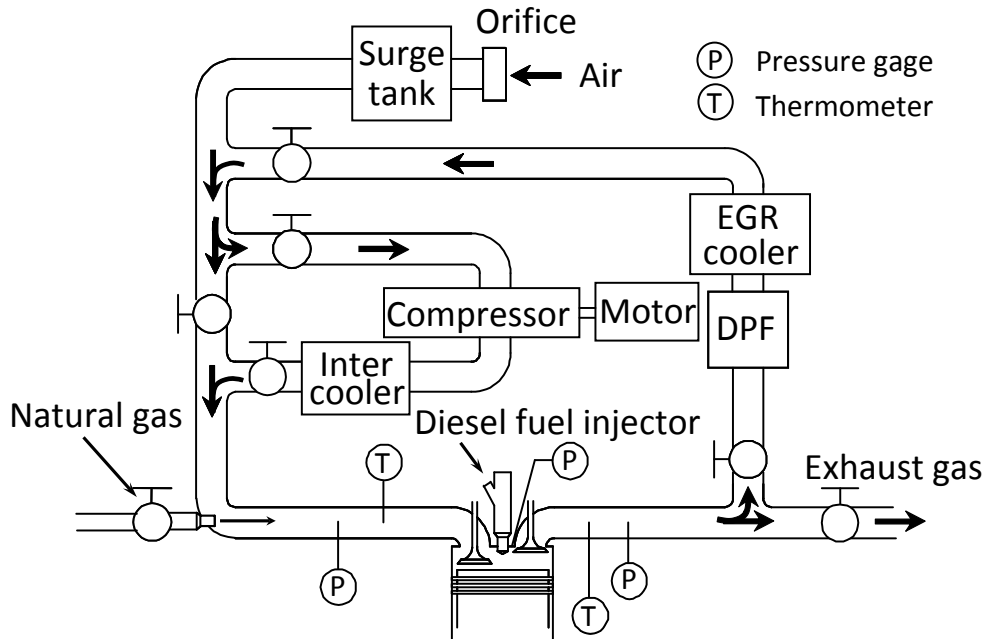
129

130 **2. Experimental setup**

131 *2.1 Engine bench test*

132 The schematic of the engine bench test is shown in Figure 1, and the specifications of the single
133 cylinder MPII natural gas engine for the present study are listed in Table 1. The detailed
134 information of the engine bench test system can be found in the previous publication [13], here
135 only a brief description is given. Natural gas was introduced into the engine from the intake
136 manifold. The micro-pilot diesel was directly injected into the cylinder by a common rail fuel
137 injection system with 120 MPa injection pressure. The diesel injector has nine holes with the
138 orifice diameter of 0.16 mm and the spray included angle of 152° . The injection duration was
139 2.53°CA , resulting in an injection quantity of 4.0×10^{-3} ml/cycle. An injection timing of
140 $-7.30^\circ\text{CA ATDC}$, which was an optimized one with a consideration of the thermal efficiency as
141 high as possible and the maximum rate of pressure rise below $1.2\text{MPa}/^\circ\text{CA}$, was employed to
142 calibrate the simulation models for optimization of the combustion chamber. For the data at
143 other injection timings, one may refer to the previous publication [13]. The supercharger driven

144 by an electric motor, and EGR system connected with a diesel particulate filter (DPF) and an
 145 EGR inter-cooler were adopted in the system. In order to eliminate the influences from the
 146 pumping process, the exhaust back pressure in the exhaust manifold was automatically regulated
 147 by an electric controlled throttle to keep the same as the intake manifold pressure.



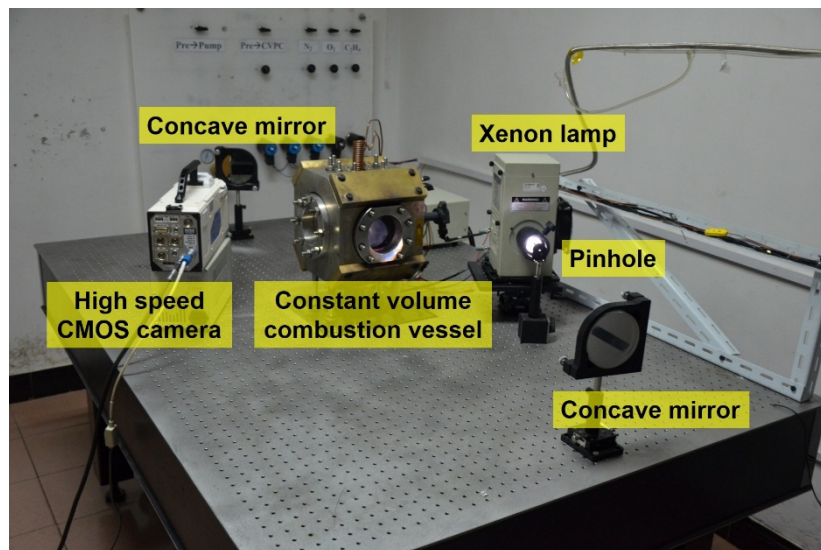
148
 149 **Fig. 1.** Schematic diagram of the MPII natural gas engine.

150
 151 **Table 1.** MPII natural gas engine specifications.

Engine configuration	Single cylinder, four-stroke, direct injection
Bore × Stroke	98 × 110mm
Displacement	0.83 L
Compression ratio	16.5:1
Engine speed	1200 rpm
Equivalent ratio of natural gas	0.513
Indicated mean effective pressure (IMEP)	8.0 bar
Intake oxygen concentration	21%
Swirl ratio	1.8
Intake valve closing (IVC)	-140° CA ATDC
Exhaust valve opening (EVO)	150° CA ATDC
Injection pressure	120 MPa
Diesel injection duration	2.53° CA
Start of injection	-7.30° CA ATDC
Diesel fuel volume per shot	4.0×10^{-3} ml/cycle

152 **2.2 Spray visualization test**

153 As shown in Figure 2, a Z-type experimental setup for the high-speed Shadowgraph imaging
154 technique was established for the spray characterization to calibrate the spray model. It consisted
155 of a Xenon lamp (Newport 66984), a pinhole, two concave mirrors and a high-speed CMOS
156 video camera (NAC Memrecam HX-6). The imaging speed of 50000 fps (frame per second) was
157 used to record the temporal and spatial development of the micro-pilot diesel spray under the
158 non-evaporating conditions. The same injector as that in the engine bench tests was used and a
159 specially designed cap was install on the injector tip to enable only one hole fuel injection by a
160 high-pressure common-rail system.



161
162 **Fig. 2.** Experiment setup of Shadowgraph imaging technique for the micro-pilot diesel spray
163 under the non-evaporating conditions.

164
165 The fuel injection and ambient conditions in this study are given in Table 2. The high
166 pressure constant-volume vessel was charged with nitrogen (N_2) to the targeted ambient density
167 for the test of non-evaporating diesel spray. The method proposed by Naber and Siebers [21]
168 was adopted to determine the tip penetration length of the diesel spray.

169

Table 2. Test conditions for the non-evaporating diesel fuel spray.

Ambient gas density ρ_a	20 kg/m ³
Ambient gas temperature T_a	298 K
Injection pressure P_{inj}	120 MPa
Injection duration t_d	0.55 ms/shot
Fuel temperature T_f	298 K

170

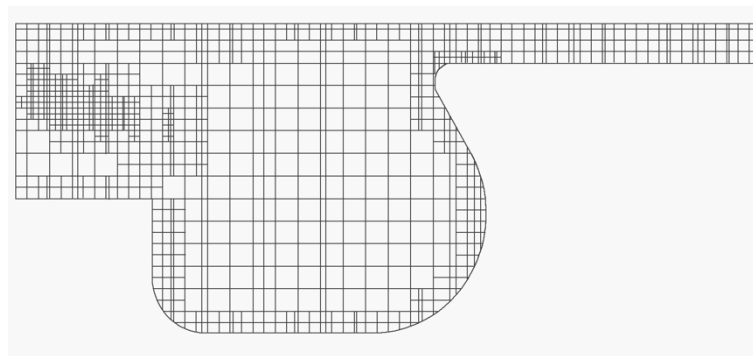
171 **3. Numerical model and validation**

172 **3.1 3D CFD modeling**

173 The 3D CFD numerical model for the engine combustion simulation was established based
174 on CONVERGETM software package. In order to implement the detailed chemistry calculations
175 and analyses during the combustion simulation process, the detailed transient chemistry solver,
176 termed as SAGE, was incorporated into the 3D CFD model. The standard CHEMKIN format
177 files used to define the chemical mechanisms and thermodynamic properties can be directly
178 resolved by SAGE solver. In the model, the premixed natural gas oxidation process was
179 represented using the GRI-Mech 3.0 chemical kinetic mechanism [22], while the chemical
180 reactions of diesel fuel were represented by those of the surrogates developed by Farrel et al.
181 [23]. Finally, the merged chemical kinetic mechanism consisted of 76 species and 464 reactions.
182 Renormalization Group (RNG) $k-\varepsilon$ turbulence model based on the Reynolds Averaged
183 Navier-Stokes (RANS) theory was used to simulate the turbulent flow within the combustion
184 chamber [24]. Compared with the standard $k-\varepsilon$ turbulence model, the turbulence dissipation rate
185 affected by the velocity dilatation and the variation of kinematic viscosity was taken into account
186 in the RNG $k-\varepsilon$ turbulence model [25]. The combustion model proposed by Kong et al. [26] was
187 employed in this study to determine the kinetic and turbulent time scales in the simulation.

188 The break-up processes of short-pulsed diesel spray was simulated by the Kelvin-Helmholtz
189 and Rayleigh-Taylor (KH-RT) hybrid model using the physical properties of DF2. The droplet
190 collision processes were simulated by the No Time Counter (NTC) method [27], Frossling
191 correlation was used to calculate the vaporization rate of liquid droplets [28]. Although no
192 droplet impingements would occur because of the short-pulsed injection in this study, the wall
193 film model proposed by O'Rourke and Amsden was employed in the simulation [29]. Woschni's
194 model was employed to simulate the heat transfer in this study [30]. The extended Zel'dovich
195 mechanism was utilized to describe the NOx formation [31]. The prediction of soot formation
196 and oxidation was not considered in the present study, since the amount of soot formed in the
197 MPII natural gas engine was not discernable in the previous experimental study [13].

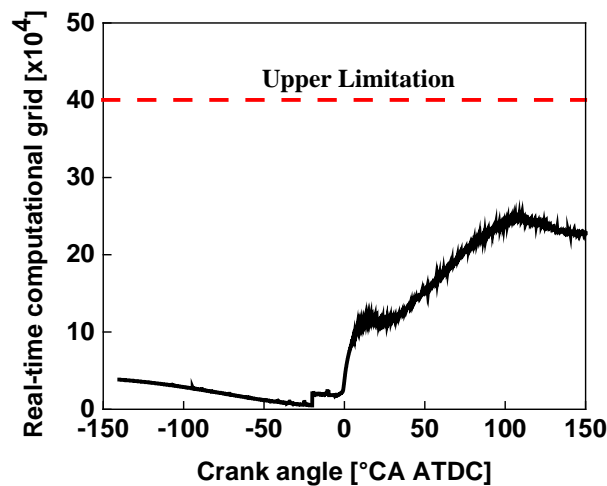
198 Due to the symmetry of the combustion chamber and injector with the nine nozzle holes, a
199 40° sector mesh was used to reduce the computational burden. The base grid was set to 1.4 mm.
200 Figure 3 shows the computational mesh used in this study, and the simulation was carried out
201 with the closed system from IVC at -140° CA ATDC to EVO at 150° CA ATDC.



202
203 **Fig. 3.** 40° sector computational mesh of the baseline engine.

204 In order to simplify the grid generation for moving boundaries, an adaptive mesh refinement
205 (AMR) algorithm was used to obtain the improved accuracy with acceptable computational cost.
206 Furthermore, the local mesh embedding technique, such as in the near-injector region, was

207 adopted as well [32]. The maximum upper limitation of the total orthogonal hex volume mesh
208 element generated was set to 400, 000 during the entire combustion simulation procedure. Figure
209 4 displays the evolution of the real-time computational grid number with crank angle in the
210 present study.



211
212 **Fig. 4.** The evolution of the real-time computational grid number with crank angle during the
213 entire combustion simulation procedure.

214

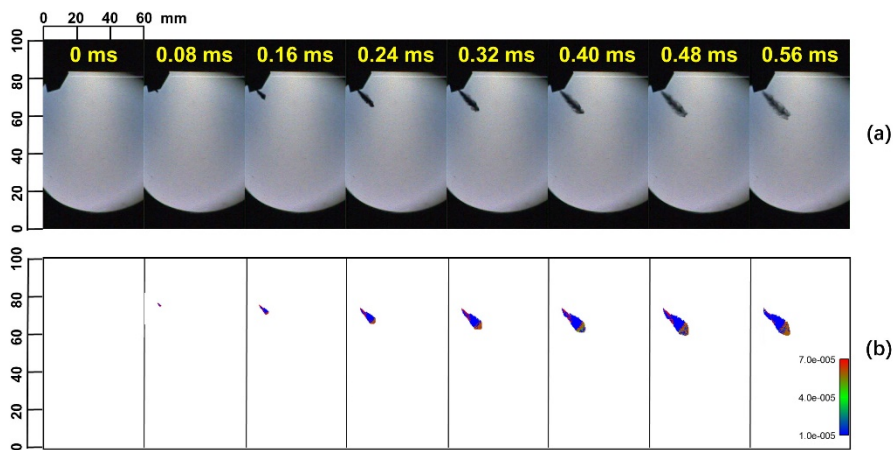
215 *3.2 Spray model validation*

216 It is well known that the temporal and spatial development of diesel spray has the critical
217 impacts on the combustion characteristics and emissions formation of diesel engines. Although
218 the injection amount of the micro-pilot diesel is small, the accuracy of spray model is also
219 considered to be crucial for the MPII natural gas engine. In this work, the calibration of the
220 micro-pilot diesel spray model was conducted based on the experimental results of the
221 non-evaporating diesel spray in the high pressure constant-volume vessel.

222 Figure 5(a) shows the high speed Shadowgraph images of the diesel spray under the high
223 ambient pressure and room temperature conditions. Given at the top of each image is the time
224 after start of the fuel injection (ASOI). Since the same 9-hole injector as used in the engine

225 bench tests was employed here, a specially designed cap was mounted at the tip of the nozzle to
 226 block the interference from the sprays issued by other holes, and only one spray plume is imaged
 227 in Figure 5(a).

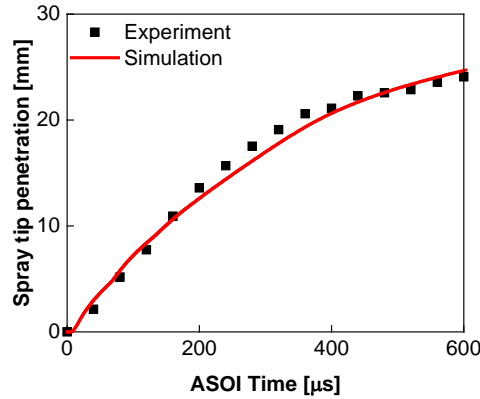
228 Under the same conditions as the spray test, the micro-pilot diesel spray in the high pressure
 229 constant-volume vessel was simulated using CONVERGE™ software package. The spray angle
 230 was kept at 15° based on the experimental results. In the simulation, the threshold which is 99.9%
 231 of the fuel mass fraction remains was used to determine the spray tip penetration length. The
 232 internal flow was not considered in the simulation, so we simplified the geometry by neglecting
 233 the nozzle tip or using a virtual position where fuels were issued out. Figure 5(b) shows the
 234 temporal development of the simulated short-pulsed spray under the same injection and ambient
 235 conditions. A reasonable agreement between the simulation and experiments can be found in
 236 Figure 5.



237 **Fig. 5.** The temporal development of short-pulsed diesel spray under the non-evaporating
 238 conditions: (a) high speed Shadowgraph images, (b) CFD simulation results ($t_d = 0.55$ ms,
 239 $P_{inj}=120$ MPa, $T_a=298$ K, $\rho_a=20$ kg/m³).

241 The comparison of experiment and simulation results for micro-pilot diesel spray tip
 242 penetration is shown in Figure 6. Through tuning the relative coefficients in the KH-RT hybrid
 243 breakup model, the temporal development of micro-pilot diesel spray in the simulation is well

244 consistent with the experimental results. Therefore, the calibrated micro-pilot diesel spray model
 245 can be applied to the followed engine CFD simulation.



246
 247 **Fig. 6.** Comparison of measured and predicted spray tip penetrations for the micro-pilot diesel
 248 fuel ($t_d = 0.55$ ms, $P_{inj} = 120$ MPa, $T_a = 298$ K, $\rho_a = 20$ kg/m³).

249 **3.3 Engine CFD model validation**

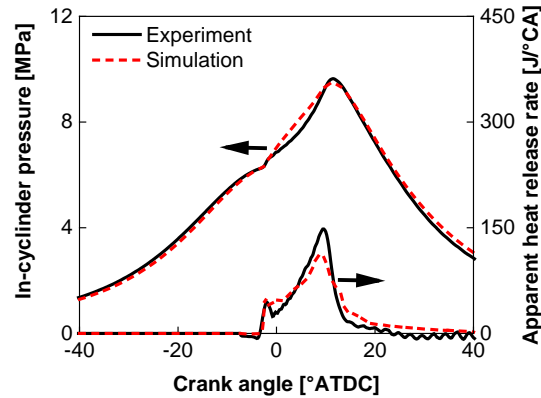
250 Natural gas is composed primarily of methane, but may also contain ethane, propane and
 251 heavier hydrocarbons. Small quantities of nitrogen may also be found in the natural gas. Table 3
 252 provides the composition of the 13A natural gas in Japan, which is the same as that in the
 253 experiments [13].

254 **Table 3.** Natural gas compositions in percent volume.

CH ₄	89.91%
C ₂ H ₆	4.42%
C ₃ H ₈	4.61%
n-C ₄ H ₁₀	0.51%
i-C ₄ H ₁₀	0.45%
i-C ₅ H ₁₂	0.03%
N ₂	0.07%

255
 256 Prior to optimization of the engine operating conditions and the combustion bowl geometry,
 257 the 3D CFD engine simulation model must be validated against the experimental results,
 258 including the cylinder pressure trace, the rate of heat release, and the exhaust gas emissions.

259 Figure 7 shows the comparison of in-cylinder pressure history and apparent heat release rate
260 (AHRR) between the experiment and simulation. As shown in this figure, the predicted pressure
261 history and AHRR agrees reasonably well with the experimental results.



262
263 **Fig. 7.** Model validation for in-cylinder pressure history and apparent heat release rate
264 (IMEP=8.0 bar, $n=1200$ rpm, $V_{DF}=4.0\times 10^{-3}$ ml/cycle, $\Phi_{NG}=0.513$).

265
266 The predicted pollutant emissions including HC, CO, and NOx emissions are compared with
267 the experimental emissions in Figure 8. A reasonably well agreement between the simulation
268 and experimental data is also achieved for the HC and CO emissions. A relatively large
269 deviation of the calculated result from the experimental result is observed for the NOx emissions.
270 Since the objective of this study is to reduce HC and CO emissions, only extended Zel'dovich
271 NOx mechanism (i.e. Thermal NOx) was employed in the simulation to reduce the computation
272 cost. The decreased combustion temperature in the lean operation of MPII engine would make it
273 more significant the prompt NOx which produced at relatively low temperature. That could be
274 the reason for the large deviations of NOx calculation, but further investigations are needed to
275 clarify this issue. Since the primary target of this study is to reduce the HC and CO emissions by
276 optimization of the combustion chamber geometry, the calibrated simulation models are believed
277 to be effective to do the work in this study.

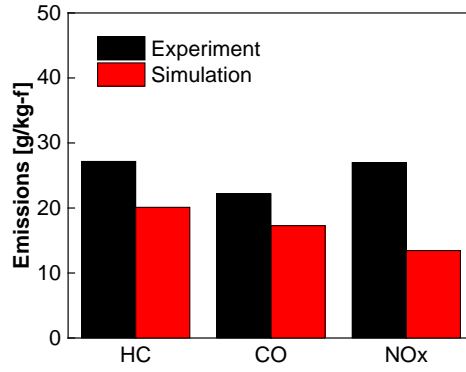


Fig. 8. Comparisons of emissions between simulation and experiments (IMEP=8.0 bar, $n=1200$ rpm, $V_{DF}=4.0 \times 10^{-3}$ ml/cycle, $\Phi_{NG}=0.513$).

4. Model-based optimization methodology

4.1 Parameterization of combustion chamber geometry

In order to obtain the variable combustion chamber geometries, the outline of the piston bowl needs to be parameterized. In this study, the two cubic Bezier functions were employed to describe the piston bowl geometry [33-35], as shown in Figure 9. In this work, compression ratio was kept constant for all the cases with varying R_{bowl} . Therefore, the volume of the piston bowl, cylinder bore, engine stroke, and the height of squish zone are not changed during optimization.

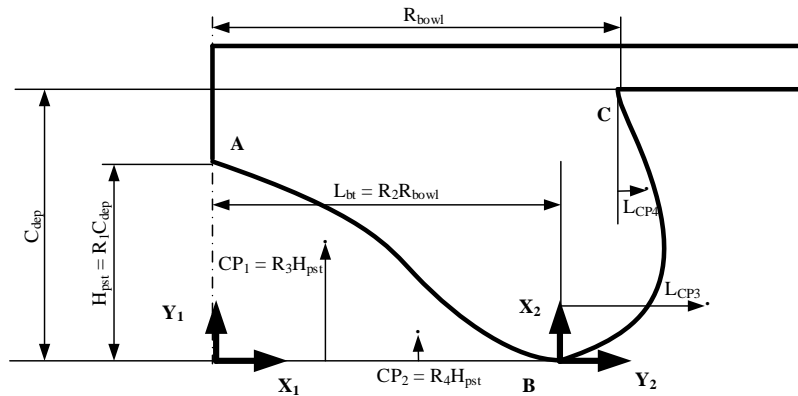


Fig. 9. The parameterized combustion chamber geometry by two Bezier functions.

As shown in Figure 9, the bowl geometry is separated into two cubic Bezier curves, i.e., one from point A to point B, the other from point B to point C. The equations can be described as follows:

$$\begin{cases}
X_1(t) = t \times L_{bt} \\
Y_1(t) = (1-t)^3 H_{pst} + 3(1-t)^2 t CP_1 + 3(1-t)t^2 CP_2 \\
X_2(t) = t \times C_{dep} \\
Y_2(t) = 3(1-t)^2 t L_{CP3} + 3(1-t)t^2 L_{CP4} + t^3 (R_{bowl} - L_{bt})
\end{cases} \quad (1)$$

295 where $t \in [0, 1]$.

296 For the sake of simplicity R_3 and R_4 are 1.1 and 0, respectively, for all the cases in the
297 present study.

298

299 **4.2 Design of experiment and meta-modeling**

300 The optimization algorithm is sometimes coupled with the full model (i.e., the sophisticated
301 CFD simulation model in this study) to explore the total available design space [36, 37].

302 However, it will lead to the excessive consumption of the computational time and efforts.

303 Therefore, in this work, the CFD simulation model of the MPII natural gas engine was replaced
304 by the high-fidelity meta-model to engage the optimization procedure.

305 Based on the combination of innovative space-filling criteria and specialized optimization
306 schemes [38, 39], the optimized Latin hypercube sampling strategy (OLHS), served as a kind of
307 excellent technique of Design of Experiment (DOE), was employed in the present study.

308 Compared to the conventional Latin hypercube sampling method, OLHS, as a more efficient
309 sampling strategy, requires fewer sample points and achieves a specific level of accuracy [40].

310 The design variables and corresponding ranges are listed in Table 4.

311 **Table 4.** Design variables and corresponding ranges.

Design variable	Range
C_{dep}	14 - 25 mm
R_1	0.3 - 0.7
R_2	0.5 - 0.8

L_{CP3}	10 - 20 mm
L_{CP4}	-10 - 10 mm
Injection timing	-15 - -5 °CA ATDC
Included spray angle	140° - 170°

312

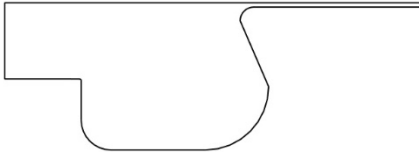
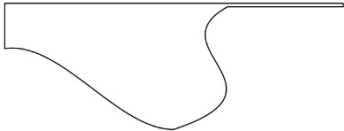
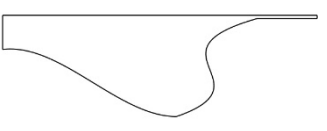
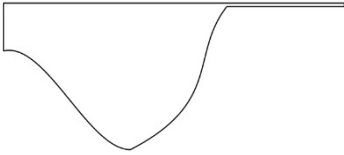
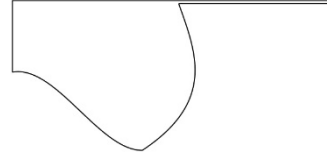
313 In this study, a total of 80 sampling points were generated by the OLHS method. Figure 10

314 depicts the typical combustion chamber geometries, including the re-entrant, shallow bowl,

315 open-crater and deep bowl types based on the proposed sampling points. It means that the

316 proposed methodology is capable of creating most of the bowl shapes considered in practical

317 diesel engines.

Baseline				
DOE results	Re-entrant type		Shallow bowl type	
	$C_{dep}=17.53\text{mm}$ $R_1=0.7582$ $R_2=0.6595$ $L_{cp3}=17.97\text{mm}$ $L_{cp4}=-2.91\text{mm}$		$C_{dep}=15.25\text{mm}$ $R_1=0.6823\text{mm}$ $R_2=0.6848\text{mm}$ $L_{cp3}=14.81\text{mm}$ $L_{cp4}=-5.44\text{mm}$	
	Open-crater type		Deep bowl type	
	$C_{dep}=20.44\text{mm}$ $R_1=0.5684$ $R_2=0.6899$ $L_{cp3}=13.29\text{mm}$ $L_{cp4}=8.48\text{mm}$		$C_{dep}=22.34\text{mm}$ $R_1=0.781$ $R_2=0.5329$ $L_{cp3}=11.27\text{mm}$ $L_{cp4}=8.23\text{mm}$	

318 **Fig. 10.** Typical combustion chamber geometries from 80 sampling points generated by the
319 optimized Latin hypercube sampling strategy.

320

321 Based on the DOE results, the meta-model of the MPII natural gas engine CFD code was

322 established by three different approximation techniques, including the Kriging method [41],

323 response surface method (RSM) [42] and artificial neural networks (ANN) method [43],

324 respectively. Here, Root Mean Square Error (RMSE) and Maximum Absolute Error (MAX)

325 served as commonly used validation metrics for the different meta-models are listed in Table 5
 326 [44]. Accordingly, the results show that the Kriging method can provide a higher predicted
 327 accuracy, compared to the other methods. It is therefore applied into the following optimization
 328 procedure.

329 **Table 5.** Validation metrics for different meta-models.

Meta-model	Kriging		RSM		ANN	
	<i>RMSE</i>	<i>MAX</i>	<i>RMSE</i>	<i>MAX</i>	<i>RMSE</i>	<i>MAX</i>
Gross indicated thermal efficiency η_i (%)	0.120	0.203	0.342	0.650	0.210	0.419
HC emissions (g/kg-f)	0.197	0.215	0.410	0.722	0.307	0.805
CO emissions (g/kg-f)	0.181	0.216	0.269	0.509	0.250	0.492
NOx emissions (g/kg-f)	0.102	0.213	0.201	0.458	0.304	0.775

330

331 **4.3 Multi-objective optimization for chamber geometry**

332 In the present study, the optimization objectives were set to minimize the HC and CO
 333 emissions, while the gross indicated thermal efficiency η_i , NOx emissions and maximum rate of
 334 pressure rise $(dP/d\theta)_{\max}$ were treated as the constraint conditions, as shown in Equation (2):

$$\left\{ \begin{array}{l} \text{Optimization objectives :} \\ \quad \text{Minimum HC and CO emissions} \\ \text{Constraint conditions :} \\ \quad \eta_i \geq \eta_{i\text{baseline}}, \text{ NOx} \leq \text{NOx}_{\text{baseline}}, (dP/d\theta)_{\max} \leq 1.2\text{MPa}/^\circ\text{CA} \end{array} \right. \quad (2)$$

336 where $\eta_{i\text{baseline}}$ and $\text{NOx}_{\text{baseline}}$ are respectively the gross indicated thermal efficiency and NOx
 337 emissions of the engine in the experiments.

338 Therefore, the multi-objective evolutionary algorithm (MOEA) based on the principles of
 339 natural evolutionary in biological systems [44] was used to resolve the proposed design
 340 optimization problem. As one of the most prevalent MOEAs [45, 46], NSGA- II with the elitist
 341 strategy and diversity preserving mechanism was adopted in this work.

342

343 5. Results and discussion

344 5.1 Optimal results of the combustion chamber geometry

345 The optimal results of the design objectives and constraint conditions obtained by the
346 multi-objective optimization algorithm NSGA-II are listed in Table 6. After optimization, the
347 HC emissions has been substantially decreased from 16.38 g/kg-f to 7.13 g/kg-f. In addition,
348 another optimal objective, the CO emissions, has a reduction of about 33.55%. Simultaneously,
349 the NOx emissions, gross indicated thermal efficiency η_i have been slightly improved, and the
350 maximum rate of pressure rise $(dP/d\theta)_{\max}$ have been slightly increased.

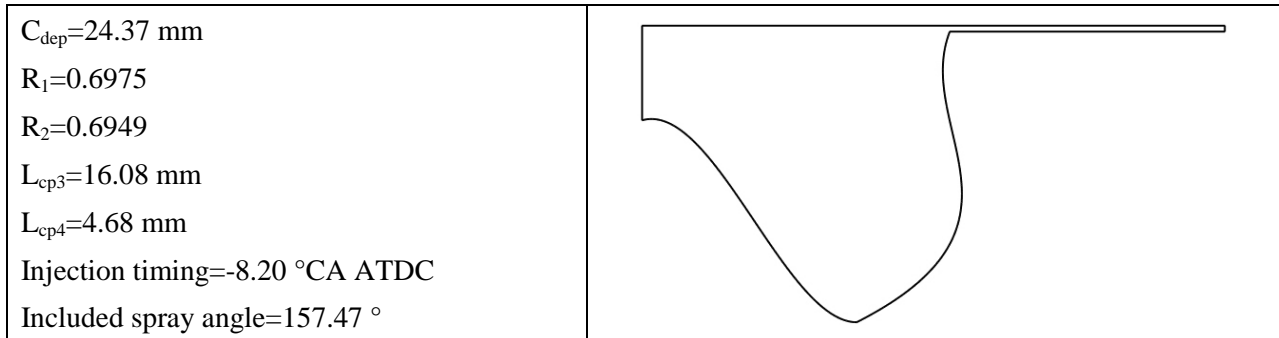
351 **Table 6.** The comparison between baseline case and optimum case.

	Item	Baseline	Optimum	Variation
Objectives	HC emissions (g/kg-f)	16.38	7.13	-56.47 %
	CO emissions (g/kg-f)	14.07	9.35	-33.55 %
Constraints	NOx emissions (g/kg-f)	10.96	10.82	-1.28 %
	Gross indicated thermal efficiency (%)	42.77	43.31	+1.26 %
	Maximum rate of pressure rise (MPa/°CA)	1.17	1.19	+1.71 %

352

353 Figure 11 illustrates the optimal results of design variables and the corresponding
354 combustion chamber geometry. Compared to the baseline case, the cup depth C_{dep} has increased
355 from 16.70 mm to 24.37 mm, which is 45.93% larger than its original depth. However, the inlet
356 diameter of the combustion chamber R_{bowl} is reduced from 27.70 mm to 25.87 mm. As a result,
357 the surface area/volume ratio of optimal combustion chamber is 0.185mm^{-1} , which is 11.06%
358 less than that of the baseline case. As well-known, it is beneficial that the less surface
359 area/volume ratio will decrease the heat transfer loss during the engine operating process,

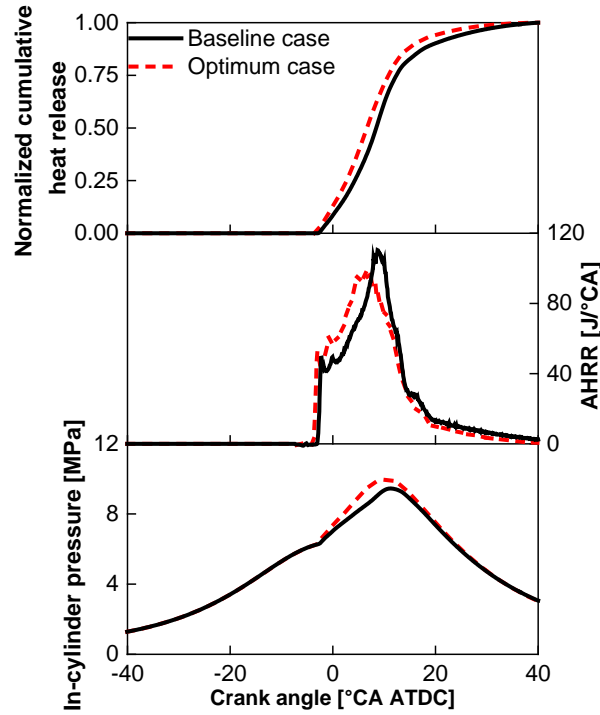
360 increasing the thermal efficiency. Additionally, the optimum engine operating conditions include
 361 an advanced diesel injection timing of $-8.20^{\circ}\text{CA ATDC}$ and a wider included spray angle of
 362 157.47° in comparison to the baseline case.



363 **Fig. 11.** Optimal design variables and the corresponding combustion chamber geometry based
 364 on NSGA- II multi-objective optimization algorithm.

365

366 As depicted in Figure 12, the in-cylinder pressure trace, AHRRs and normalized cumulative
 367 heat release of the baseline and optimum cases are shown together. It can be seen that the high
 368 temperature reaction of optimum case started slightly earlier than that of the baseline case. As a
 369 result, the optimal CA50 (crank angle of 50% accumulative heat released) combustion phasing
 370 for the 8.0 bar IMEP operation is found to be $6.65^{\circ}\text{CA ATDC}$. Compared to the original
 371 $8.50^{\circ}\text{CA ATDC@CA50}$, the optimal combustion phasing is closer to the top dead center of the
 372 piston, leading to the higher degree of constant volume heat release during the combustion
 373 process. Combined with the less surface area/volume ratio, the fuel economy of optimum case
 374 will be further improved. In addition, as to the optimum case, the maximum value of AHRR
 375 represents a 12.49% reduction in comparison to the baseline case. However, the peak in-cylinder
 376 pressure through the optimization has been slightly increased from 9.45 MPa to 9.94 MPa. That
 377 means the thermal efficiency of the MPII natural gas engine is not deteriorated for the optimum
 378 case.



379

380

381

Fig. 12. Comparisons of the in-cylinder pressure history, apparent heat release rate and normalized cumulative heat release between optimum case and baseline case.

382

383

384

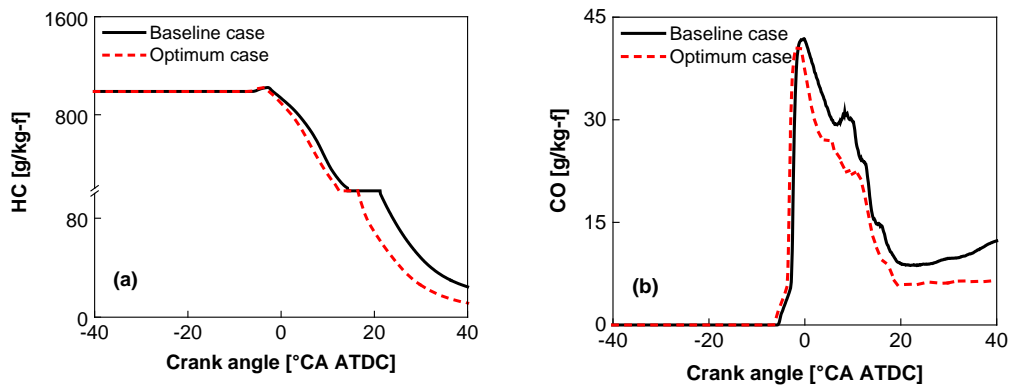
385

386

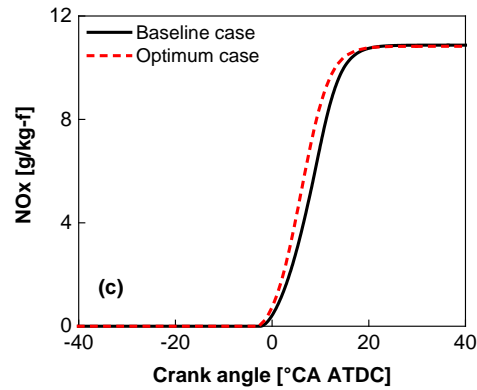
387

388

In the cases of HC and CO emissions, as shown in Figure 13(a) and (b), the evolution trends with the crank angle for the optimum and baseline cases seem to be similar. However, the production amount of HC/CO emissions for the optimum case are significantly reduced at the same crank angle position after top dead center compared to the baseline. Furthermore, the NO_x emission of the optimum case is comparable to that of the baseline case, as shown in Figure 13(c).



389



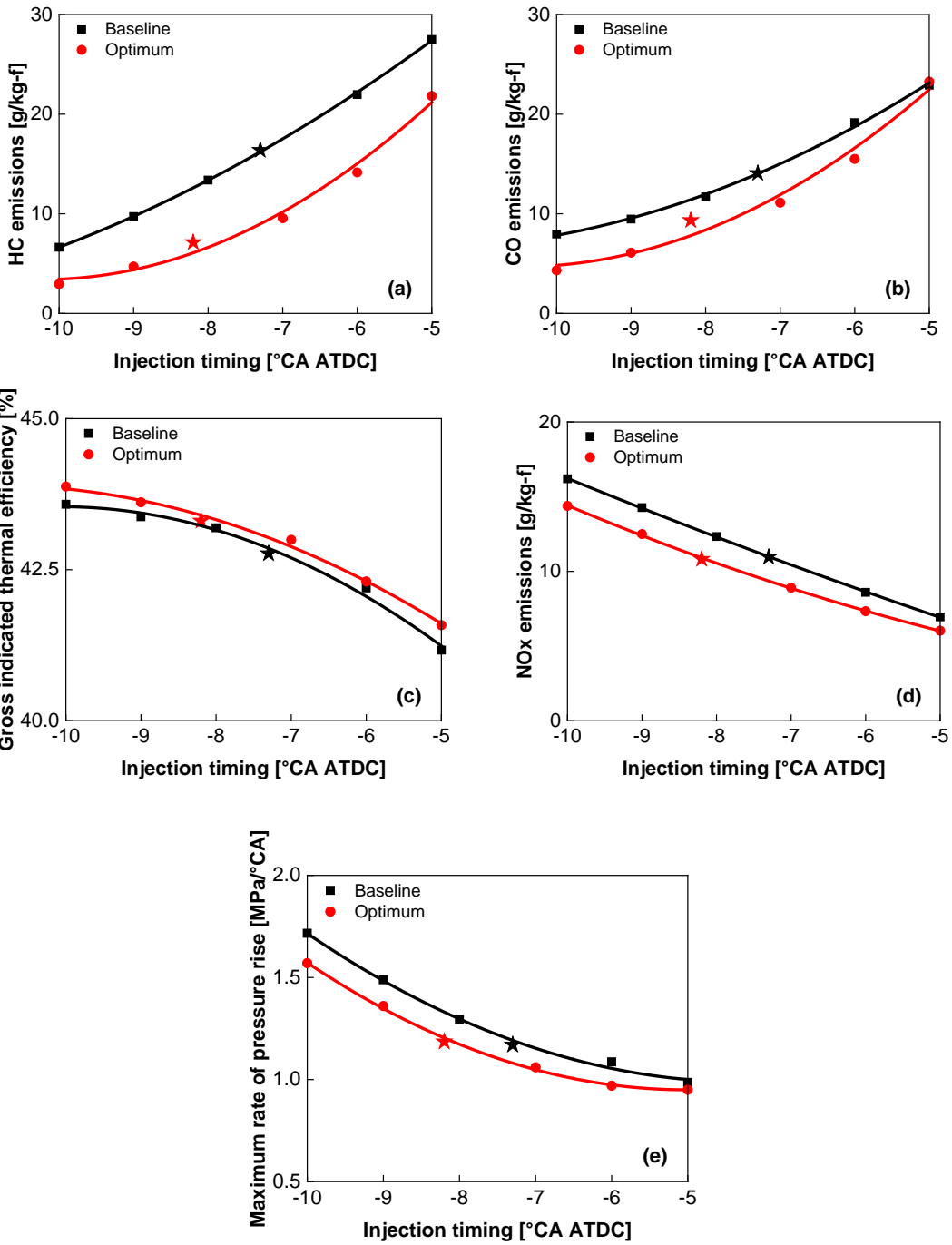
390
 391 **Fig. 13.** Comparisons of the exhaust gas emission characteristics between optimum and baseline
 392 cases.

393

394 CFD simulations of the MPII natural gas engine with the diesel fuel injection timing swept
 395 from -10 to -5°CA ATDC under the same conditions as in Figure 13 were conducted, the results
 396 are depicted in Figure 14. The black star represents the level of baseline case using -7.30°CA
 397 ATDC injection timing, the red star denotes the optimum case with -8.20°CA ATDC injection
 398 timing, and the black and red curves indicate the data trend with the injection timing sweep.

399 With fixed injection timing, compared to the baseline case, both the HC, CO and NOx emissions
 400 are lower, and the thermal efficiency is slightly higher for the optimized combustion chamber.

401 As the injection timing of diesel fuel is advanced, though the HC and CO emissions decrease
 402 and the gross indicated thermal efficiency increase, the NOx emissions and maximum rate of
 403 pressure rise also increase. As a result of the NOx emissions and 1.2 MPa/°CA maximum rate of
 404 pressure rise constraints, the optimized result goes to the injection timing as shown by the red
 405 star in Figure 14.



406

407

408

409

410

411

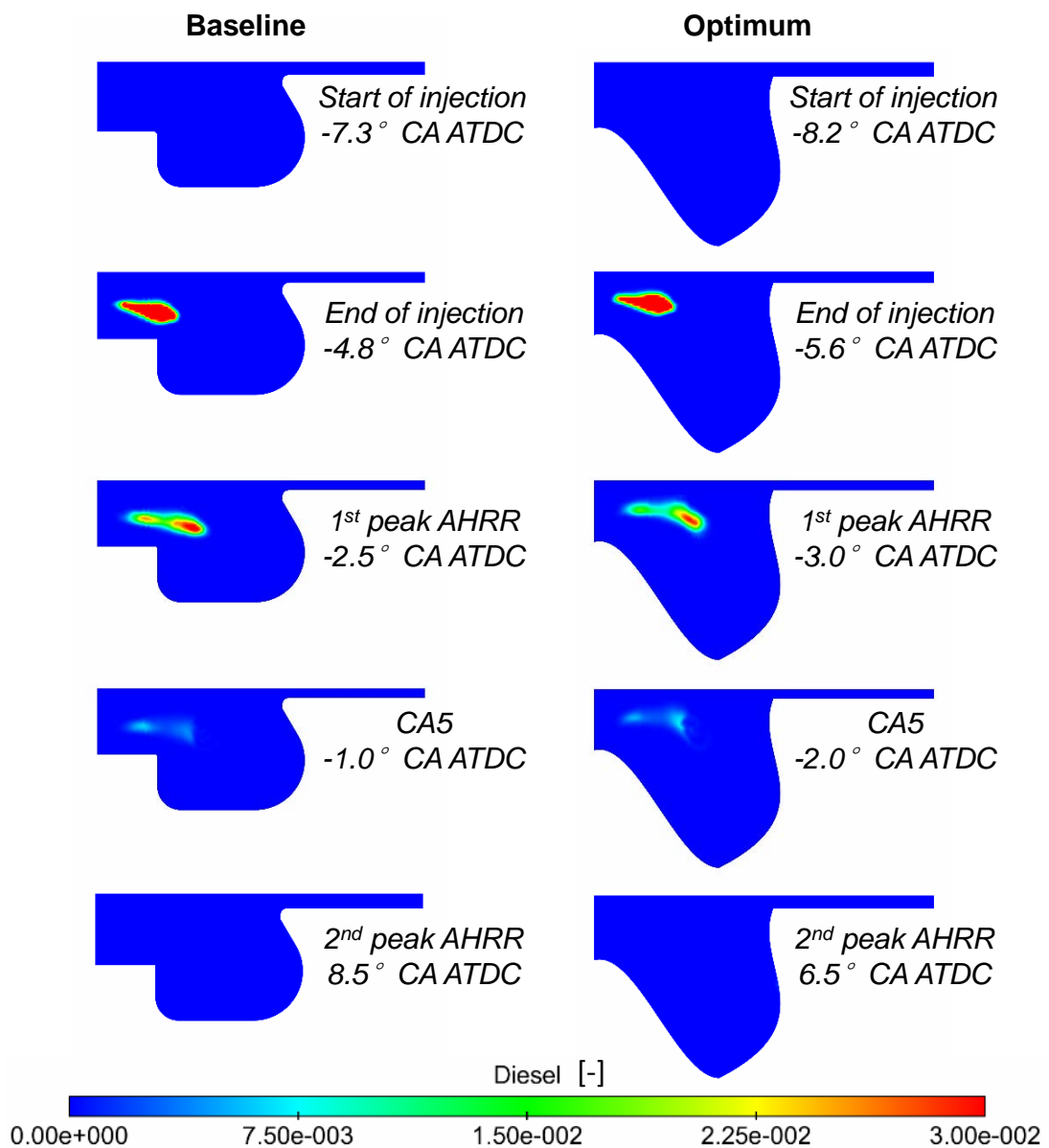
412

413

Fig. 14. Comparisons of exhaust emissions, thermal efficiency and maximum rate of pressure rise at injection timing sweep of short-pulsed diesel fuel.

5.2 Analysis of the in-cylinder flow, HC/CO and temperature distributions

414 Figure 15 represents the in-cylinder distribution of the diesel fuel at the selected crank angles.
 415 Since the injection amount of the short-pulsed diesel is small, the dilution process of diesel fuel
 416 is proceeded quickly under the entrainment movement between the diesel spray and in-cylinder
 417 ambient gas flow. As shown in Figure 15, after CA5, the diesel fuel concentration almost can't
 418 be observed any more.



419
 420
 421

Fig. 15. Contour plots of diesel fuel mole fraction at selected crank angles.

422 In addition, the combustion of the MPII natural gas engine for either the baseline or optimum
423 case is started after the end of diesel fuel injection. Consequently, the premixed auto-ignition
424 combustion of diesel fuel causes the rapid heat release rate at the initial stage, as depicted in
425 Figure 12. In this study, the equivalent ratio of natural gas is set to 0.513, which will not produce
426 the obvious soot emissions. Furthermore, the premixed combustion of diesel fuel help suppress
427 the soot formation as well. That is the reasons why the amount of soot formed in the MPII
428 natural gas engine was not discernable in the previous experimental study [13].

429 Figure 16 compares the temperature distribution in the cylinder between the baseline and
430 optimum cases. As illustrated in Figure 16, ignition initially occurs at the leading zone of the
431 short-pulsed diesel spray. Then, the burning zone is rapidly expanded to the surrounding region
432 of high reactivity that is comprised primarily of the mixture of diesel fuel and natural gas. Here
433 whether the rapid expansion of the burning zone is attributed to a propagation of regular flame or
434 a propagation of auto-ignition as suggested in the previous paper [13] is not clear, and further
435 exploration are needed to clarify this issue in the future. As to the optimum case, the area of
436 regions with temperature higher than 2200 K is comparable with that of the baseline case. That
437 is the reasons why the NO_x emissions were not deteriorated after the optimization. It is
438 noteworthy that at the CA95, there are still some unburned end gases in the center of combustion
439 chamber of the baseline case besides the squish zone. In contrast, the unburned region of the
440 optimum case only exists in the squish zone, where there are larger area with the temperature
441 above 1700 K. This would lead to reduced unburned HC and CO emissions, which will be
442 depicted in details in Figure 17 and Figure 18.

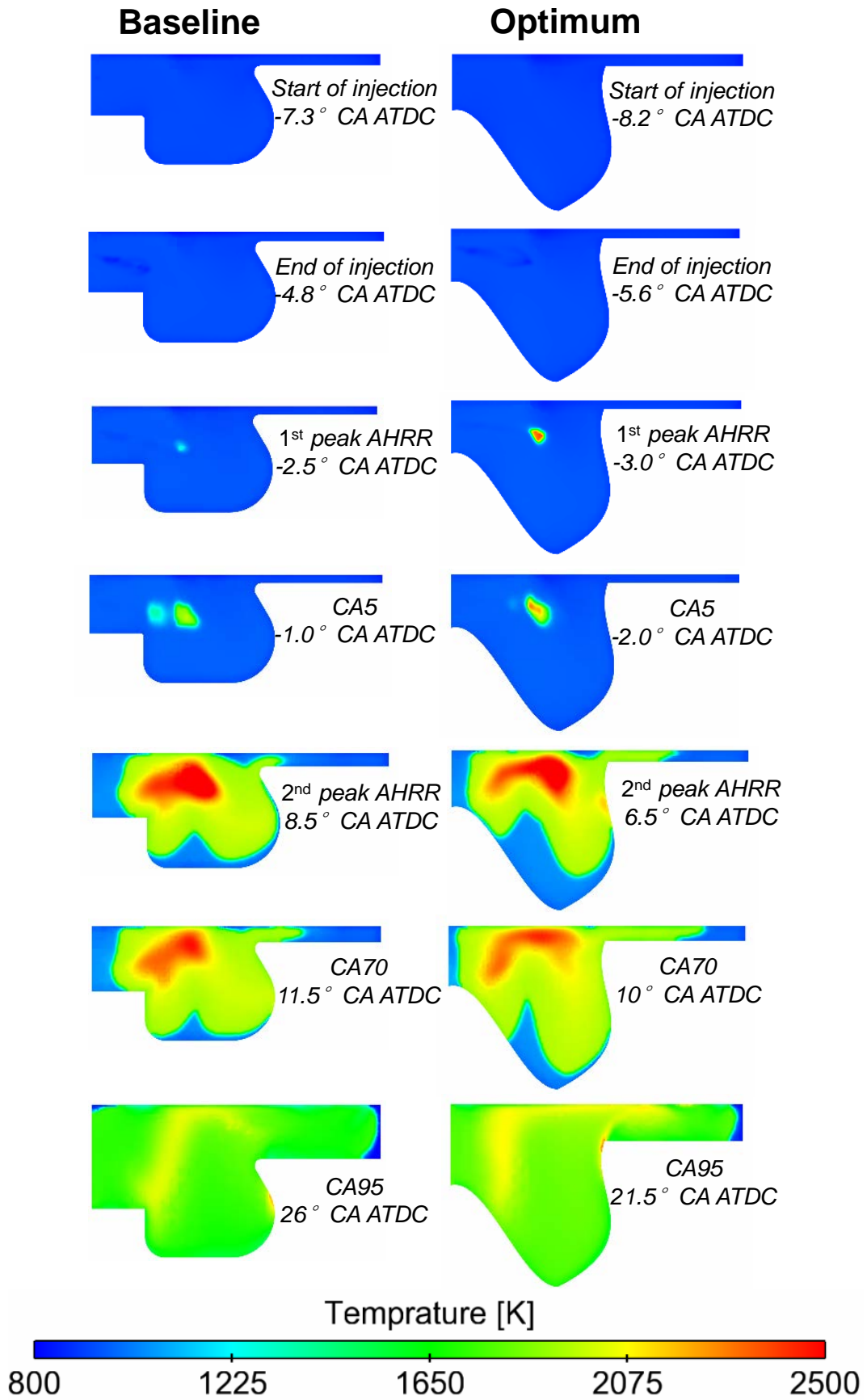
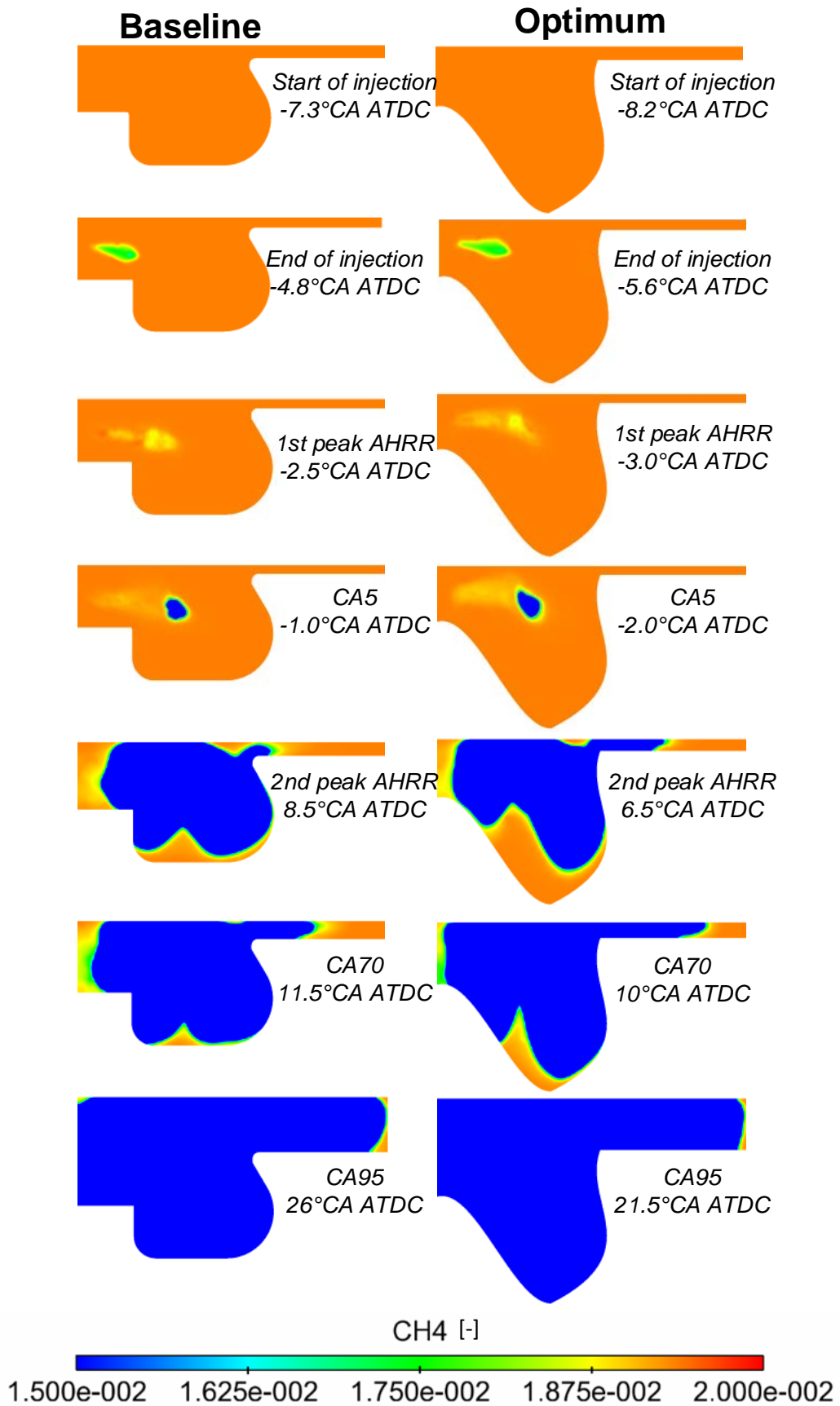


Fig. 16. Distribution of in-cylinder temperature at selected crank angles.

443
444

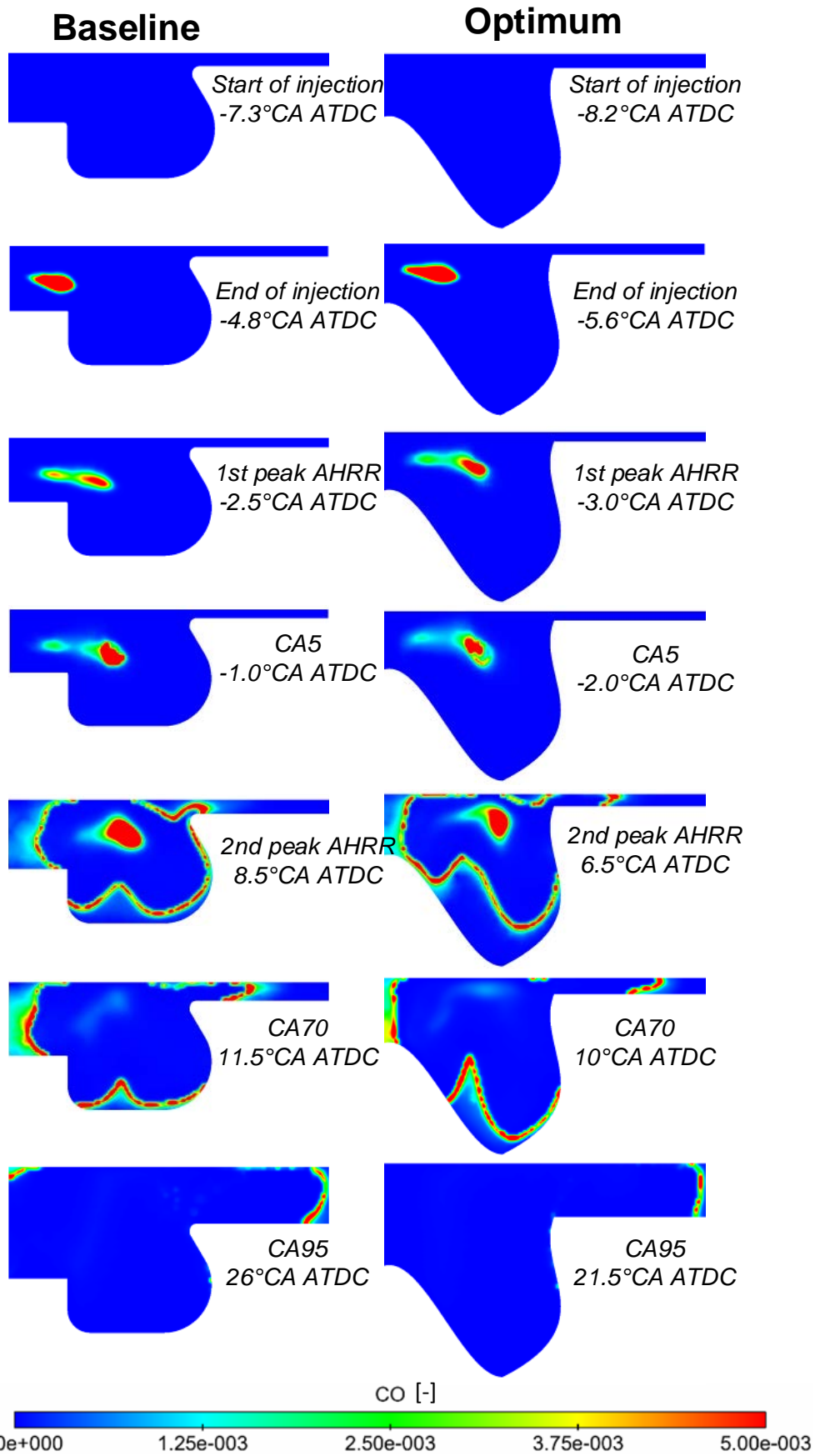
445 Figures 17 and 18 depict the contour plots of the CH₄ and CO emissions in the cylinder. Here
446 the unburned HC, which is multi-component mixture, is represented by CH₄ as the major
447 component of the unburned HC. Initially, the natural gas (i.e., unburned HC) is entrained into the
448 diesel spray, then burned with the auto-ignition of the diesel fuel. Therefore, the HC emissions in
449 the MPII natural gas engine would stem primarily from the unburned region, as shown in Figure
450 17. However, the low temperature oxidation reaction of diesel fuel at the end of injection firstly
451 produces an amount of CO emissions. With the flame propagation, the CO emissions are
452 produced at the flame front, as depicted in Figure 18.

453 At the end of the combustion (i.e., CA95), there exists HC and CO in both the chamber
454 center and the squish zone in the baseline case. In comparison to the baseline case, only the
455 squish zone have some HC and CO emissions, and their occupied area is remarkably reduced.



456
457

Fig. 17. Contour plots of the CH₄ mole fraction at selected crank angles.

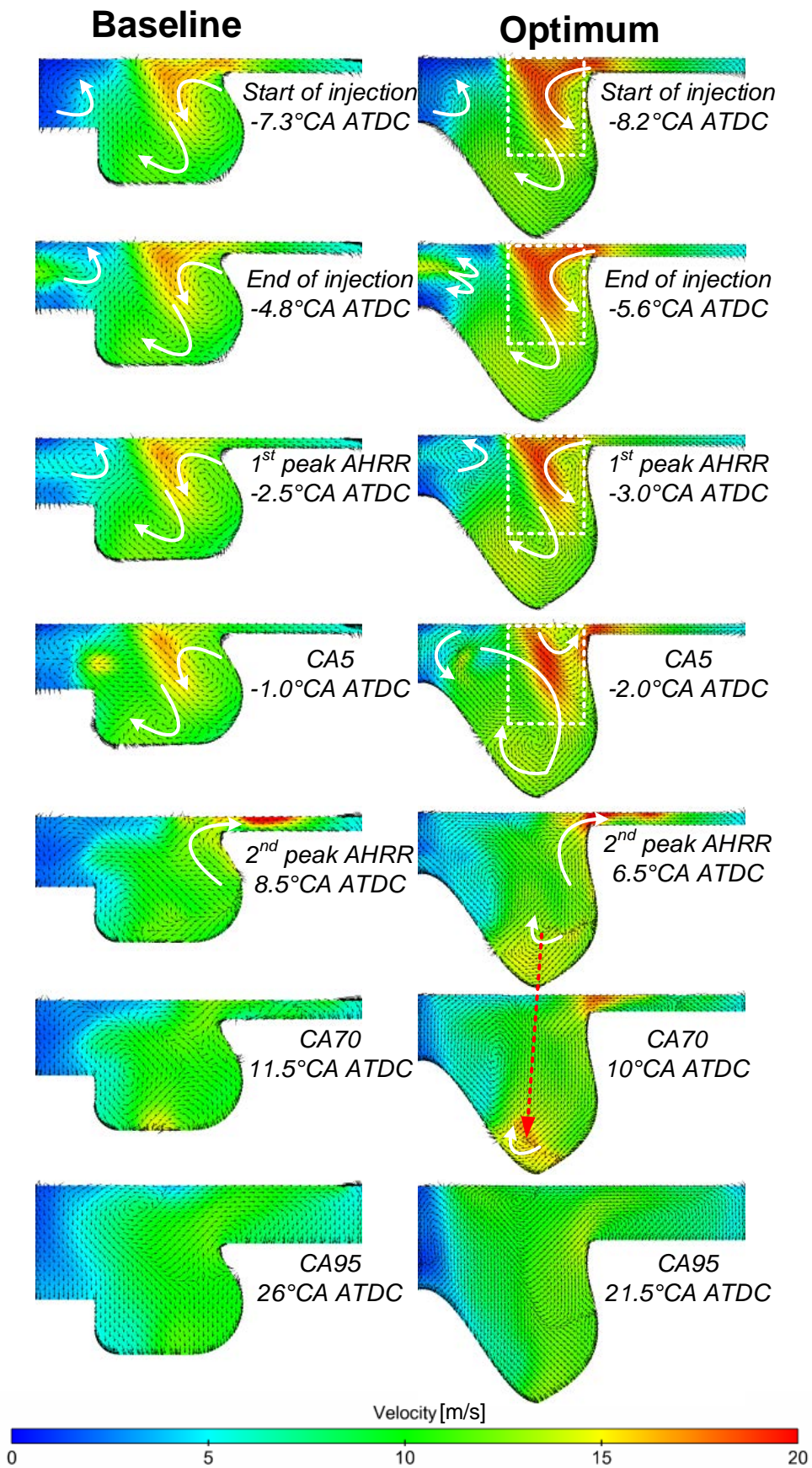


458

459

Fig. 18. Contour plots of the CO mole fraction at selected crank angles.

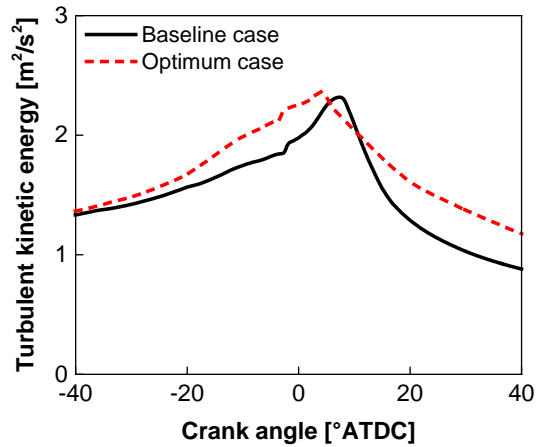
460 To further understand the behavior of HC and CO distribution, the in-cylinder distribution of
461 the flow field at the selected crank angles are shown in Figure 19. Here the color bar is
462 employed to represent the strength of flow field, the black thin arrows only denote the direction
463 of the in-cylinder flow and the primary flow structures are highlighted by the white thick arrow
464 in Figure 19. In the optimum case, there are two counter-rotating vortex structures at the leading
465 edge of the micro-pilot diesel spray. These vortex structures might help promote the fuel and
466 ambient air mixing. Before TDC, owing to the larger area of piston top land in the squish zone
467 for the optimum case, the squish flow as shown in the dashed box in Fig. 19 is apparently
468 stronger than that of the baseline case. Moreover, while there are a clockwise tumble flow in the
469 piston bowl for both cases, it is stronger in the optimum case than the baseline case. After TDC,
470 with the piston moving downward, the clockwise tumble flow carries the stronger squish flow
471 into the bottom region of the piston bowl and then moves toward the center region of the
472 chamber, resulting in stronger turbulence for the optimum case than the baseline case.
473 Meanwhile, the anti-squish flow toward the squish zone is enforced by the larger area of piston
474 top land in the squish zone for the optimum case, compared to the baseline case. As a
475 consequence, the in-cylinder kinetic energy in the optimum case is higher for almost the whole
476 combustion period, compared to the baseline case, as depicted in Figure 20. This could be the
477 reason why the HC and CO emissions are reduced by optimization of the combustion chamber
478 geometry.



479

480

Fig. 19. The in-cylinder flow field at selected crank angles.



481 **Fig. 20.** The in-cylinder turbulent kinetic energy in the optimum and baseline cases.
 482

483

484 6. Conclusions

485 In the present study, optimization of the combustion chamber geometry and the engine

486 operating conditions for natural gas engines with diesel micro-pilot-induced ignition were

487 implemented using the NSGA- II multi-objective evolutionary algorithm, aiming at reductions

488 in the HC and CO emissions and improvement in the combustion efficiency. The major results

489 are summarized as follows:

490 • The computational results of the proposed CFD model agree reasonably well with the

491 experimental results, and a variety of combustion chamber geometries can be generated

492 by the parameterized Bezier functions.

493 • With the proposed optimization methodology based on the Kriging meta-model and

494 optimized Latin hypercube sampling strategy, the HC and CO emissions are reduced by

495 56.47 % and 33.55 %, respectively. The gross indicated thermal efficiency, the NOx

496 emissions and the maximum rate of pressure rise, which were used as constraints in the

497 optimization, are to some degree improved.

- 498 • Ignition occurs at the leading edge after end of the micro-pilot diesel injection, then the
499 burning zone expands quickly over the highly reactive diesel and nature gas mixture.
500 However, whether the auto-ignition or regular flame propagation dominates the process
501 is still not clear, and further exploration is needed to clarify this issue in the future.
- 502 • The increased thermal efficiency is attributed to the smaller surface area/volume ratio and
503 higher degree of constant volume heat release, while the slightly improved NO_x and
504 maximum rate of pressure rise could be due to the faster mixing by the micro-pilot diesel
505 spray and ambient gas in the optimum case, compared to the baseline case.
- 506 • The greater tumble flow with the deep bowl and the stronger squish flow and anti-squish
507 flow owing to the larger area of piston top land in the squish zone greatly enhance the
508 in-cylinder turbulent kinetic energy, resulting in the reduced HC and CO emissions in the
509 optimum case, compared to the baseline case.

510

511 **Acknowledgement**

512 The supports by the Natural Science Foundation of China (51276115 & 91541104) and the
513 Funding by SKL Ocean Engineering (GKZD010065&GKZD010068) are gratefully
514 acknowledged.

515

516 **References**

517 [1] Lamaris VT, Hountalas DT. A general purpose diagnostic technique for marine diesel
518 engines - application on the main propulsion and auxiliary diesel units of a marine vessel.
519 Energy Convers Manage 2010; 51(4): 740-53.

- 520 [2] Hountalas DT. Prediction of marine diesel engine performance under fault conditions.
521 Applied Thermal Engineering 2000; 20(18): 1753-83.
- 522 [3] Herdzik J. Emissions from marine engines versus IMO certification and requirements of tier
523 3. Journal of KONES 2011; 18: 161-7.
- 524 [4] Park SH, Lee CS. Applicability of dimethyl ether (DME) in a compression ignition engine as
525 an alternative fuel. Energy Convers Manage 2014; 86: 848-63.
- 526 [5] Yousefi A, Biroukb M, Lawlerc B, Ghareghania A. Performance and emissions of a
527 dual-fuel pilot diesel ignition engine operating on various premixed fuels. Energy Convers
528 Manage 2015; 106: 322-36.
- 529 [6] Li T, Moriwaki R, Ogawa H, Kakizaki R, Murase M. Dependence of premixed
530 low-temperature diesel combustion on fuel ignitability and volatility. International Journal of
531 Engine Research 2012; 13(1): 14-27.
- 532 [7] Yang B, Wei X, Xi CX, Liu Y, Zeng K, Lai MC. Experimental study of the effects of natural
533 gas injection timing on the combustion performance and emissions of a turbocharged
534 common rail dual-fuel engine. Energy Convers Manage 2014; 87: 297-304.
- 535 [8] U.S. Energy Information Administration. International energy statistics. 2015.
536 <<http://www.eia.gov/cfapps/ipdbproject/IEDIndex3.cfm?tid=3&pid=3&aid=1>>. [accessed
537 on 13. Dec. 2015].
- 538 [9] Cho HM, He BQ. Spark ignition natural gas engines - a review. Energy Convers Manage
539 2007; 48(2): 608-18.
- 540 [10] Liao SY, Cheng Q, Jiang DM, Gao J. Experimental study of flammability limits of natural
541 gas - air mixture. Journal of Hazardous Materials 2005; 119(1-3): 81-4.

- 542 [11]Kato K, Igarashi K, Masuda M, Otsubo K, et al. Development of engine for natural gas
543 vehicle. SAE technical paper 1999-01-0574; 1999.
- 544 [12]Reyes M, Tinaut FV, Giménez B, Pérez A. Characterization of cycle-to-cycle variations in a
545 natural gas spark ignition engine. Fuel 2015; 140(0): 752-61.
- 546 [13]Ogawa H, Zhao PL, Kato T, Shibata G. Improvement of combustion and emissions in a dual
547 fuel compression ignition engine with natural gas as the main fuel. SAE technical paper
548 2015-01-0863; 2015.
- 549 [14]Reitz RD, Duraisamy G. Review of high efficiency and clean reactivity controlled
550 compression ignition (RCCI) combustion in internal combustion engines. Progress in Energy
551 and Combustion Science 2015; 46(0): 12-71.
- 552 [15]Takahashi S, Goto S, Nakayama S, Nishi Y. Result in Service operation of 1.3MW
553 micro-pilot gas engine, and its future development. CIMAC Congress; Paper No.146; 2004.
- 554 [16]Tsunoda A, Yamamoto T, Dexter S. Further development of advanced gas engine KU30GA
555 (MACH-30A). CIMAC Kongress; Paper No. 120; 2004.
- 556 [17]Abdelaal MM, Hegab AH. Combustion and emission characteristics of a natural gas-fueled
557 diesel engine with EGR. Energy Convers Manage 2012; 64: 301-12.
- 558 [18]Papagiannakis RG, Hountalas DT. Combustion and exhaust emission characteristics of a
559 dual fuel compression ignition engine operated with pilot Diesel fuel and natural gas. Energy
560 Convers Manage 2004; 45(18-19): 2971-87.
- 561 [19]Liu J, Yang FY, Wang HW, Ouyang MG, Hao SG. Effects of pilot fuel quantity on the
562 emissions characteristics of a CNG/diesel dual fuel engine with optimized pilot injection
563 timing. Applied Energy 2013; 110: 201-6.

- 564 [20]Ishiyama T, Jeongho K, Yutaka O, Takahiro S. Improvement of performance and reduction
565 of exhaust emissions by pilot-fuel-injection control in a lean-burning natural-gas dual-fuel
566 engine. SAE Int. J. Fuels Lubr. 2011; 5(1): 243-53.
- 567 [21]Naber JD, Siebers DL. Effects of gas density and vaporization on penetration and dispersion
568 of diesel sprays. SAE technical paper 1996-02-01; 1996.
- 569 [22]Smith GP, Golden DM, Frenklach M, Moriarty NW, Eiteneer B, Goldenberg M, Lissianski
570 VV. GRI-Mech 3.0. 1999. <http://combustion.berkeley.edu/gri-mech/>. [accessed on 13. Dec.
571 2015].
- 572 [23]Farrell JT, Cernansky NP, Dryer FL, Law CK, Friend DG, Hergart CA, McDavid RM, Patel
573 AK, Mueller CJ, Pitsch H. Development of an experimental database and kinetic models for
574 surrogate diesel fuels. SAE technical paper 2007-01-0201; 2007.
- 575 [24]Han Z, Reitz RD. Turbulence modeling of internal combustion engines using RNG κ - ϵ
576 models. Combustion Science and Technology 1995; 106(4-6): 267-95.
- 577 [25]Kong SC, Han Z, Reitz RD. The development and application of a diesel ignition and
578 combustion model for multidimensional engine simulation. SAE technical paper 950278;
579 1995.
- 580 [26]Kong SC, Marriott CD, Reitz RD, Christensen M. Modeling and experiments of HCCI
581 engine combustion using detailed chemical kinetics with multidimensional CFD. SAE
582 technical paper 2001-01-1026; 2001.
- 583 [27]Schmidt DP, Rutland CJ. A new droplet collision algorithm. Journal of Computational
584 Physics 2000; 164(1): 62-80.

585 [28]Amsden AA, O'Rourke PJ, Butler TD. KIVA-II: a computer program for chemically
586 reactive flows with sprays. Los Alamos National Laboratory Report No. LA-11560-MS;
587 1989.

588 [29]O'Rourke PJ, Amsden AA. A spray/wall interaction submodel for the KIVA-3 wall film
589 model. SAE technical paper 2000-01-0271; 2000.

590 [30]Woschni G. A universally applicable equation for the instantaneous heat transfer coefficient
591 in the internal combustion engine. SAE technical paper 670931; 1967.

592 [31]Patterson M, Kong S, Hampson G, Reitz R. Modeling the effects of fuel injection
593 characteristics on diesel engine soot and NOx emissions. SAE technical paper 940523; 1994.

594 [32]Schmitt T, Méry Y, Boileau M, Candel S. Large-Eddy Simulation of oxygen/methane
595 flames under transcritical conditions. Proceedings of the Combustion Institute 2011; 33(1):
596 1383-90.

597 [33]Park SW. Optimization of combustion chamber geometry for stoichiometric diesel
598 combustion using a micro genetic algorithm. Fuel Processing Technology 2010; 91(11):
599 1742-52.

600 [34]Shi Y, Reitz RD. Assessment of optimization methodologies to study the effects of bowl
601 geometry, spray targeting and swirl ratio for a heavy-duty diesel engine operated at high-load.
602 SAE Int. J. Engines 2008; 1(1): 537-57.

603 [35]Park S. Optimization of combustion chamber geometry and engine operating conditions for
604 compression ignition engines fueled with dimethyl ether. Fuel 2012; 97(0): 61-71.

605 [36]Ge HW, Shi Y, Reitz RD, Wickman D, Willems W. Engine development using
606 multi-dimensional CFD and computer optimization. SAE technical paper 2010-01-0360;
607 2010.

608 [37]Rajabi MM, Ataie-Ashtiani B, Janssen H. Efficiency enhancement of optimized Latin
609 hypercube sampling strategies: application to Monte Carlo uncertainty analysis and
610 meta-modeling. *Advances in Water Resources* 2015; 76: 127-39.

611 [38]Wołoszyn J, Gołaś A. Sensitivity analysis of efficiency thermal energy storage on selected
612 rock mass and grout parameters using design of experiment method. *Energy Convers
613 Manage* 2014; 87: 1297-304.

614 [39]Park J, Lee KS, Kim MS, Jung D. Numerical analysis of a dual-fueled CI (compression
615 ignition) engine using Latin hypercube sampling and multi-objective Pareto optimization.
616 *Energy* 2014; 70: 278-87.

617 [40]Monger SH, Morgan ER, Dyreson AR, Acker TL. Applying the Kriging method to
618 predicting irradiance variability at a potential PV power plant. *Renewable Energy* 2016; 86:
619 602-10.

620 [41]Abbaszadeh K, Alam FR, Saied SA. Cogging torque optimization in surface-mounted
621 permanent-magnet motors by using design of experiment. *Energy Convers Manage* 2011;
622 52(10): 3075-82.

623 [42]Piloto-Rodríguez R, Sánchez-Borroto Y, Lapuerta M, Goyos-Pérez L, Verhelst S. Prediction
624 of the cetane number of biodiesel using artificial neural networks and multiple linear
625 regression. *Energy Convers Manage* 2013; 65: 255-61.

- 626 [43]Shan S, Wang GG. Survey of modeling and optimization strategies to solve
627 high-dimensional design problems with computationally-expensive black-box functions.
628 Structural and Multidisciplinary Optimization 2010; 41(2): 219-41.
- 629 [44]Marler RT, Arora JS. Survey of multi-objective optimization methods for engineering.
630 Structural and Multidisciplinary Optimization 2004; 26(6): 369-95.
- 631 [45]Coello CAC. Evolutionary multi-objective optimization: a historical view of the field. IEEE
632 Computational Intelligence Magazine 2006; 1(1): 28-36.
- 633 [46]Deb K, Pratap A, Agarwal S, Meyarivan T. A fast and elitist multi-objective genetic
634 algorithm: NSGA-II. IEEE Transactions on Evolutionary Computation 2002; 6(2): 182-97.